 CMES, vol.44, no.2, pp.137-155, 2009

Consistent Boundary Conditions for 2D and 3D Lattice Boltzmann Simulations

Chih-Fung Ho[1], Cheng Chang[1], Kuen-Hau Lin[1] and Chao-An Lin[1] [2]

Abstract: Consistent formulations of 2D and 3D pressure and velocity boundary conditions along both the stationary and non-stationary plane wall and corner for lattice Boltzmann simulations are proposed. The unknown distribution functions are made function of local known distribution functions and correctors, where the correctors at the boundary nodes are obtained directly from the definitions of density and momentum. This boundary condition can be easily implemented on the wall and corner boundary using the same formulation. Discrete macroscopic equation is also derived for steady fully developed channel flow to assess the effect of the boundary condition on the solutions, where the resulting second order accurate central difference equation predicts continuous distribution across the boundary provided the boundary unknown distribution functions satisfy the macroscopic quantity. Three different local known distribution functions are experimented to assess both this observation and the applicability of the present formulation, and are scrutinized by calculating two-dimensional Couette-Poiseuille flow, Couette flow with wall injection and suction, lid-driven square cavity flow, and three-dimensional square duct flow. Numerical simulations indicate that the present formulation is second order accurate and the difference of adopting different local known distribution functions is as expected negligible, which are consistent with the results from the derived discrete macroscopic equation.

Keywords: Boundary conditions, plane wall, corner, lattice Boltzmann method.

1 Introduction

Lattice Boltzmann method (LBM) [Chen, Chen, Martinez, and Matthaeus (1991); Qian, d'Humieres, and Lallemand (1992); Chen and Doolen (1998)] has been successfully applied to various hydrodynamic problems[Chen, Martinez, and Mei

[1] Department of Power Mechanical Engineering, National Tsing Hua University, Hsinchu 30013, Taiwan.
[2] Corresponding author; calin@pme.nthu.edu.tw

(1996); Chen, Chang, and Sun (2007); Han, Feng, and Owen (2007); Chen, Lin, and Lin (2007); Chang, Liu, and Lin (2009)] and the major advantages of the LBM are explicit, easy to implement, and natural to parallelize. The LBM consists of two essential steps: collision step and streaming step. The collision step models interactions among fluid particles and the streaming step simply moves particles from one lattice to the other according to their velocities. It has been shown that at low Mach numbers the LBM solves fluid problems with second order accuracy both in space and time.

However, a successful LBM simulation rests on the correct implementation of the boundary conditions, where unknown distribution functions originated from the undefined nodes external to the flow domain are encountered during the streaming operation. The bounce-back scheme is the most popular method to handle stationary no slip wall boundaries. If the bounce-back boundary condition is implemented on the boundary nodes, where the wall resides, the bounce-back boundary condition only gives first order accuracy. However, if the bounce-back boundary condition is employed with the wall located at half-grid-spacing between a flow node and a bounce-back node, the scheme is shown to produce second-order accuracy. Nevertheless, the bounce-back scheme generates the nonzero velocity on wall boundary as long as $\tau \neq 1$ [He, Zou, Luo, and Dembo (1997)].

To obtain the unknown distribution function at the boundary, there are many approaches available [Skordos (1993); Noble, Chen, Georgiadis, and Buckius (1995); Inamuro, Yoshino, and Ogino (1995); Maier, Bernard, and Grunau (1996); Chen, Martinez, and Mei (1996); Zou and He (1997); Junk and Yang (2005)]. For example, Skordos [Skordos (1993)] proposed to calculate the boundary distribution functions using the gradients of the fluid velocity and density. In Noble et al.'s approach [Noble, Chen, Georgiadis, and Buckius (1995)], the unknown distribution functions at the boundary node are obtained directly from the definitions of density and momentum without approximations using D2Q7 lattice. On the other hand, to ensure no slip wall condition, Inamuro et al. [Inamuro, Yoshino, and Ogino (1995)] assumed that the unknown distribution functions equals the equilibrium distribution function modified with a counter slip velocity component. Both pressure and velocity boundary conditions were proposed by Maier et al. [Maier, Bernard, and Grunau (1996)], however different methodologies were employed for the velocity and pressure boundary. An extrapolation scheme was adopted by Chen et al. [Chen, Martinez, and Mei (1996)], where by adding one more layer outside the boundary, the distribution functions at this outside layer are extrapolated from internal nodes. Pressure and velocity boundary conditions were also put forward by Zou and He [Zou and He (1997)], who extended the work of Noble et al. to 2D (D2Q9) and 3D (D3Q15) flows. Due to the lattice structure adopted (D2Q9 and D3Q15), the num-

bers of unknown distribution functions exceed the number of constraint equations, therefore the bounce-back rules were assumed to be valid for the non-equilibrium distribution functions. For 3D flow, extra constraint from Maier et al. was also employed. The numerical results were shown to be approximately second-order accurate. One point boundary condition was proposed by Junk and Yang [Junk and Yang (2005)], where a correction to the bounce back boundary condition improves the accuracy of pressure and velocity.

In this paper, consistent 2D and 3D pressure and velocity boundary conditions for LBGK model are presented. The unknown distribution functions are made function of local known distribution functions and correctors. The correctors at the boundary nodes are obtained directly from the definitions of density and momentum. The present formulations can be applied to both stationary and non-stationary plane walls and corners. To assess the effect of the boundary condition on the solutions, discrete macroscopic energy equation is also derived for steady fully developed channel flow. The validity and accuracy of the new boundary condition are scrutinized by computing two-dimensional Poiseuille flow, Couette flow with mass injection and suction, and lid-driven square cavity flow. Moreover, to validate its consistent formulation to three-dimensional problem, a 3-D square duct flow is also simulated. The results show that the proposed boundary conditions can be implemented easily, and the second order accuracy is also satisfied.

2 The lattice Boltzmann equation

The lattice Boltzmann method adopting a uniform lattice with Bhatnagar-Gross-Krook collision model [Chen, Chen, Martinez, and Matthaeus (1991); Qian, d'Humieres, and Lallemand (1992); Chen and Doolen (1998)] can be expressed as,

$$f_i^+(\vec{x},t) = f_i(\vec{x},t) - \frac{1}{\tau}[f_i(\vec{x},t) - f_i^{eq}(\vec{x},t)] \tag{1}$$

$$f_i(\vec{x}+\vec{e}_i dt, t+dt) = f_i^+(\vec{x},t) \tag{2}$$

where f_i is the particle distribution function along the particle speed direction $\vec{e}_i$ and f_i^+ is the post collision particle distribution function. τ is the single relaxation time that controls the rate approaching equilibrium. The above two equations represent collision and streaming operations, respectively.

Based on the particle distribution functions, the macroscopic density and velocity are defined as:

$$\rho = \sum_i f_i \tag{3}$$

$$\rho\vec{\mathbf{u}} = \sum_i f_i\vec{e}_i \tag{4}$$

The equilibrium distribution functions, which depend on the local density and velocity, are given by the form [Qian, d'Humieres, and Lallemand (1992)],

$$f_i^{eq} = \omega_i \rho [1 + \frac{3}{c^2}\vec{e}_i \cdot \vec{u} + \frac{9}{2c^4}(\vec{e}_i \cdot \vec{u})^2 - \frac{3}{2c^2}\vec{u} \cdot \vec{u}] \tag{5}$$

where $c = dx/dt$ is the lattice speed, and dx and dt are the lattice width and time step, respectively. ω_i is a weighting factor. The speed of sound is $C_s = c/\sqrt{3}$ and the corresponding kinematic viscosity is $\nu = (\tau - 0.5)C_s^2 dt$.

For the present 2D and 3D applications, D2Q9, D3Q15 and D3Q19 models are adopted. For example, the particle speed $\vec{e}_i$ adopting D2Q9 model are defined as,

$$\vec{e}_0 = 0 \tag{6}$$

$$\vec{e}_i = (\cos[\pi(i-1)/2], \sin[\pi(i-1)/2])c \quad i = 1,2,3,4 \tag{7}$$

$$\vec{e}_i = (\cos[\pi(i-4-1/2)/2], \sin[\pi(i-4-1/2)/2])\sqrt{2}c \quad i = 5,6,7,8 \tag{8}$$

and the weighting factors are $\omega_0 = 4/9, \omega_{i=1,2,3,4} = 1/9, \omega_{i=5,6,7,8} = 1/36$.

3 Discrete forms of the macroscopic momentum and temperature equations

Before proceeding to the discussions of the boundary conditions of the lattice Boltzmaan methods, it is beneficial here to derive first the discrete forms of the macroscopic momentum and temperature equations based on the lattice Boltzmann equations, i.e. Eqs. 1 to 5. Since general discrete forms are difficult to derive, the focus here is concentrated on the D2Q9 steady fully developed channel flow driven by a fixed body force (G) with periodic boundary conditions.

The discrete Navier Stokes equation for steady fully developed channel flow has been derived by He et al. [He, Zou, Luo, and Dembo (1997)] and is expressed as,

$$\frac{u_{j+1}v_{j+1} - u_{j-1}v_{j-1}}{2\delta x} = \underbrace{\frac{2\tau - 1}{6}\frac{\delta x^2}{\delta t}}_{\nu} \frac{u_{j-1} - 2u_j + u_{j+1}}{\delta x^2} + G$$

$$+ \frac{\tau - 1}{\delta t}[\mathbf{u}_{j-1} - u_{j-1} + \mathbf{u}_{j+1} - u_{j+1}] - \frac{2\tau^2 - 2\tau + 1}{\tau \delta t}[\mathbf{u}_j - u_j] \tag{9}$$

where u and v are streamwise and transverse velocity, respectively and j is the discrete index in the transverse direction. It should be noted, however, that $\mathbf{u}$ and u are defined in Eqs. 4 and 5, respectively. Except in the boundary, $\mathbf{u} = u$. Thus the equation reduces to the second order accurate central difference equation. For

steady fully developed channel flow without transverse wall injection ($v = 0$), the equation predicts exact parabolic profiles.

The influence of the boundary condition can be verified by considering the above equation next to the lower wall, i.e.

$$\frac{u_3 v_3 - u_1 v_1}{2\delta x} = \underbrace{\frac{2\tau - 1}{6}\frac{\delta x^2}{\delta t}}_{\nu} \frac{u_1 - 2u_2 + u_3}{\delta x^2} + G + \frac{\tau - 1}{\delta t}[\mathbf{u}_1 - u_1] \tag{10}$$

where index $j = 1$ locates the lower wall. u_1 is no slip wall velocity and $\mathbf{u}_1$ is computed by the wall distribution function, i.e. $\rho \mathbf{u}_1 = C(f_1^{j=1} + f_5^{j=1} + f_8^{j=1} - f_3^{j=1} - f_6^{j=1} - f_7^{j=1})$. It is clear that $f_2^{j=1}$, $f_5^{j=1}$ and $f_6^{j=1}$ are to be determined at the wall. He et al. [He, Zou, Luo, and Dembo (1997)] concluded that, slip velocity is zero as long as $\mathbf{u}_1 = u_1$ regardless of the formulation of $f_2^{j=1}$, $f_5^{j=1}$ and $f_6^{j=1}$. This provides a guide to determine the unknown density population at the wall to be addressed in the next section. Also, since Eq. 10 involves one inhomogeneous direction only, therefore further numerical tests are adopted to asses whether this assertion is still valid for flows with two inhomogeneous directions.

4 Boundary conditions

Along the boundary, $f_i(\vec{x},t)$ due to the inward streaming operations may originate from the undefined nodes external to the flow domain, therefore measures have to be taken to prescribe these unknown particle distribution functions, which are denoted as $f_{i=p}(\vec{x},t)$. Obviously, $f_{i\neq p}(\vec{x},t) = f^+_{i\neq p}(\vec{x} - \vec{e}_i dt, t - dt)$, as shown in equation 2.

The unknown particle density distribution functions along the boundary are expressed as a combination of the local known value and a corrector,

$$f_i(\vec{x},t) = f_i^*(\vec{x},t) + \frac{\omega_i}{C}\vec{e}_i \cdot \vec{Q} \tag{11}$$

where $\vec{Q}$ is the force like corrector to enforce the required momentum. This resembles the modification of momentum due to the presence of a body force, though this only applies to the unknown particle density distribution functions along the boundary. This formulation is similar to that proposed by Maier et al. [Maier, Bernard, and Grunau (1996)] for determining the velocity boundary conditions, though with slight variation. However, as will be shown next, the present formulation can be equally applied to velocity or mixed pressure-velocity boundary and even corner for 2D and 3D flows.

For instance, consider a node at the top boundary as shown in Fig. 1, where the unknown density distribution functions are (f_4, f_7, f_8), (f_4, f_8, f_{10}, f_{11}, f_{13}) and,

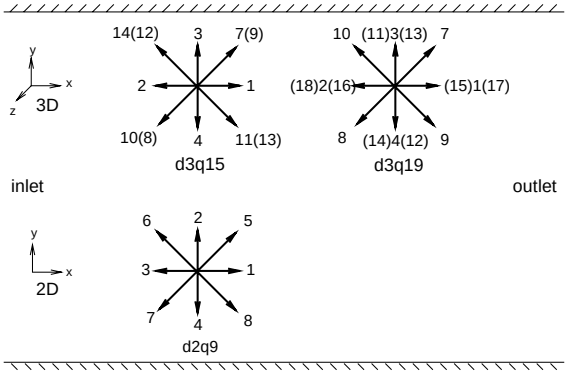

Figure 1: The 2D and 3D Lattice Boltzmann models.

(f_4, f_8, f_9, f_{12}, f_{14}) for D2Q9, D3Q15 and D3Q19 models, respectively. For D2Q9, the unknown distribution functions f_4, f_7 and f_8 can be expresses by Eq. 11, i.e. $f_4 = f_4^* - \alpha_4 Q_y$, $f_7 = f_7^* - \alpha_7(Q_x + Q_y)$ and $f_8 = f_8^* + \alpha_8(Q_x - Q_y)$. Therefore, the macroscopic velocity and density at the node using Eqs.(3) and (4), in conjunction with Eq. (11), can be expressed as,

$$\begin{aligned}
\rho &= f_0 + f_1 + f_2 + f_3 + (f_4^* - \omega_4 Q_y) + f_5 + f_6 \\
&\quad + (f_7^* - \omega_7(Q_x + Q_y)) + (f_8^* + \omega_8(Q_x - Q_y)) \\
\rho u &= f_1 + f_5 + (f_8^* + \omega_8(Q_x - Q_y)) - f_3 - f_6 - (f_7^* - \omega_7(Q_x + Q_y)) \\
\rho v &= f_2 + f_5 + f_6 - (f_4^* - \omega_4 Q_y) \\
&\quad - (f_7^* - \omega_7(Q_x + Q_y)) - (f_8^* + \omega_8(Q_x - Q_y))
\end{aligned} \tag{12}$$

If velocities u and v are known at the boundary, Eq.(12) to (12) can be used to solve for ρ, Q_x, and Q_y, and then f_4, f_7, and f_8 are obtained. The explicit forms of the unknown particle density distribution functions are shown as below.

$$\rho = \frac{f_0 + f_1 + f_3 + 2(f_2 + f_5 + f_6)}{1 + v} \tag{13}$$

$$f_4 = f_4^* - \frac{2}{3}\rho v + \frac{2}{3}(f_2 - f_4^* + f_5 - f_7^* + f_6 - f_8^*) \tag{14}$$

$$\begin{aligned} f_7 &= f_7^* - \frac{1}{2}\rho u - \frac{1}{6}\rho v + \frac{1}{2}(f_1 - f_3) \\ &+ \frac{1}{6}(f_2 - f_4^*) + \frac{2}{3}(f_5 - f_7^*) - \frac{1}{3}(f_6 - f_8^*) \end{aligned} \tag{15}$$

$$\begin{aligned} f_8 &= f_8^* + \frac{1}{2}\rho u - \frac{1}{6}\rho v - \frac{1}{2}(f_1 - f_3) \\ &+ \frac{1}{6}(f_2 - f_4^*) - \frac{1}{3}(f_5 - f_7^*) + \frac{2}{3}(f_6 - f_8^*) \end{aligned} \tag{16}$$

The local known f_i^* is still yet to be decided. As indicated from Eq. 10, as long as **u** and u, the no slip boundary condition can be ascertained. Here, three different forms of f^* are experimented to asses this assertion, i.e. $(a) : f_i^*(\vec{x},t) = f(\vec{x},-\vec{e}_i,t)$, $(b) : f_i^*(\vec{x},t) = f(\vec{x},\vec{e}_i,t-dt)$ and $(c) : f_i^*(\vec{x},t) = f^{eq}(\vec{x},\vec{e}_i,t)$. This is to investigate whether in the present formulation by satisfying the momentum, the influence of the choice of the local known distribution function f^* is negligible. For formulation (a), the present form recovers the form by Zou and He[Zou and He (1997)], and is adopted here.

The same procedure can be applied to D3Q15 and D3Q19, and the explicit forms for (f_4, f_8, f_{10}, f_{11}, f_{13}) and, (f_4, f_8, f_9, f_{12}, f_{14}), are respectively as:

For D3Q15 model,

$$\rho = \frac{f_0 + f_1 + f_2 + f_5 + f_6}{1+v} + 2\frac{f_3 + f_7 + f_9 + f_{12} + f_{14}}{1+v} \tag{17}$$

$$\begin{aligned} f_4 &= f_4^* - \frac{2}{3}\rho v + \frac{2}{3}(f_3 - f_4^* + f_7 - f_8^* + f_9 - f_{10}^* \\ &\quad + f_{12} - f_{11}^* + f_{14} - f_{13}^*) \end{aligned} \tag{18}$$

$$\begin{aligned} f_8 &= f_8^* - \frac{1}{4}\rho u - \frac{1}{12}\rho v - \frac{1}{4}\rho w + \frac{1}{4}(f_1 - f_2) + \frac{1}{4}(f_5 - f_6) + \frac{1}{12}(f_3 - f_4^*) \\ &+ \frac{7}{12}(f_7 - f_8^*) + \frac{1}{12}(f_9 - f_{10}^*) \\ &- \frac{5}{12}(f_{12} - f_{11}^*) + \frac{1}{12}(f_{14} - f_{13}^*) \end{aligned} \tag{19}$$

$$\begin{aligned} f_{10} &= f_{10}^* - \frac{1}{4}\rho u - \frac{1}{12}\rho v + \frac{1}{4}\rho w + \frac{1}{4}(f_1 - f_2) - \frac{1}{4}(f_5 - f_6) + \frac{1}{12}(f_3 - f_4^*) \\ &+ \frac{1}{12}(f_7 - f_8^*) + \frac{7}{12}(f_9 - f_{10}^*) \\ &+ \frac{1}{12}(f_{12} - f_{11}^*) - \frac{5}{12}(f_{14} - f_{13}^*) \end{aligned} \tag{20}$$

$$\begin{aligned} f_{11} &= f_{11}^* + \frac{1}{4}\rho u - \frac{1}{12}\rho v + \frac{1}{4}\rho w - \frac{1}{4}(f_1 - f_2) - \frac{1}{4}(f_5 - f_6) + \frac{1}{12}(f_3 - f_4^*) \\ &- \frac{5}{12}(f_7 - f_8^*) + \frac{1}{12}(f_9 - f_{10}^*) \\ &+ \frac{7}{12}(f_{12} - f_{11}^*) + \frac{1}{12}(f_{14} - f_{13}^*) \end{aligned} \tag{21}$$

$$\begin{aligned} f_{13} &= f_{13}^* + \frac{1}{4}\rho u - \frac{1}{12}\rho v - \frac{1}{4}\rho w - \frac{1}{4}(f_1 - f_2) + \frac{1}{4}(f_5 - f_6) + \frac{1}{12}(f_3 - f_4^*) \\ &+ \frac{1}{12}(f_7 - f_8^*) - \frac{5}{12}(f_9 - f_{10}^*) \\ &+ \frac{1}{12}(f_{12} - f_{11}^*) + \frac{7}{12}(f_{14} - f_{13}^*) \end{aligned} \tag{22}$$

For D3Q19 model,

$$\rho = \frac{f_0 + f_1 + f_2 + f_5 + f_6 + f_{15} + f_{16} + f_{17} + f_{18}}{1+v} + 2\frac{(f_3 + f_7 + f_{10} + f_{11} + f_{13})}{1+v}$$

$$\begin{aligned} f_4 &= f_4^* - \frac{1}{3}\rho v \\ &+ \frac{1}{3}(f_3 - f_4^* + f_7 - f_8^* + f_{10} - f_9^* \\ &\quad + f_{11} - f_{12}^* + f_{13} - f_{14}^*) \end{aligned} \tag{23}$$

$$\begin{aligned} f_8 &= f_8^* - \frac{1}{2}\rho u - \frac{1}{6}\rho v \\ &+ \frac{1}{2}(f_1 - f_2) + \frac{1}{2}(f_{15} - f_{16}) + \frac{1}{2}(f_{17} - f_{18}) \\ &+ \frac{1}{6}(f_3 - f_4^*) + \frac{2}{3}(f_7 - f_8^*) - \frac{1}{3}(f_{10} - f_9^*) \\ &+ \frac{1}{6}(f_{11} - f_{12}^*) + \frac{1}{6}(f_{13} - f_{14}^*) \end{aligned} \tag{24}$$

$$\begin{aligned} f_9 &= f_9^* + \frac{1}{2}\rho u - \frac{1}{6}\rho v \\ &- \frac{1}{2}(f_1 - f_2) - \frac{1}{2}(f_{15} - f_{16}) - \frac{1}{2}(f_{17} - f_{18}) \\ &+ \frac{1}{6}(f_3 - f_4^*) - \frac{1}{3}(f_7 - f_8^*) + \frac{2}{3}(f_{10} - f_9^*) \\ &+ \frac{1}{6}(f_{11} - f_{12}^*) + \frac{1}{6}(f_{13} - f_{14}^*) \end{aligned} \tag{25}$$

$$\begin{aligned} f_{12} &= f_{12}^* - \frac{1}{6}\rho v - \frac{1}{2}\rho w \\ &+ \frac{1}{2}(f_5 - f_6) + \frac{1}{2}(f_{15} - f_{16}) - \frac{1}{2}(f_{17} - f_{18}) \\ &+ \frac{1}{6}(f_3 - f_4^*) + \frac{1}{6}(f_7 - f_8^*) + \frac{1}{6}(f_{10} - f_9^*) \\ &+ \frac{2}{3}(f_{11} - f_{12}^*) - \frac{1}{3}(f_{13} - f_{14}^*) \end{aligned} \tag{26}$$

$$\begin{aligned} f_{14} &= f_{14}^* - \frac{1}{6}\rho v + \frac{1}{2}\rho w \\ &- \frac{1}{2}(f_5 - f_6) - \frac{1}{2}(f_{15} - f_{16}) + \frac{1}{2}(f_{17} - f_{18}) \\ &+ \frac{1}{6}(f_3 - f_4^*) + \frac{1}{6}(f_7 - f_8^*) + \frac{1}{6}(f_{10} - f_9^*) \\ &- \frac{1}{3}(f_{11} - f_{12}^*) + \frac{2}{3}(f_{13} - f_{14}^*) \end{aligned} \tag{27}$$

The same procedure can be applied to D3Q15 and D3Q19 models for a node at the left boundary, and the unknown particle distribution functions are (f_1, f_7, f_9, f_{11}, f_{13}) and, (f_1, f_7, f_9, f_{15}, f_{17}), respectively. It is possible to obtain explicit form of the unknown particle distribution functions as shown below.

For D3Q15 model,

$$\begin{aligned} u &= 1 - \frac{f_0 + f_3 + f_4 + f_5 + f_6}{\rho} \\ &\quad +2\frac{f_2 + f_8 + f_{10} + f_{12} + f_{14}}{\rho} \end{aligned} \tag{28}$$

$$\begin{aligned} f_1 &= f_1^* + \frac{2}{3}\rho u \\ &+ \frac{2}{3}(f_2 - f_1^* + f_8 - f_7^* + f_{10} - f_9^* \\ &\quad +f_{12} - f_{11}^* + f_{14} - f_{13}^*) \end{aligned} \tag{29}$$

$$\begin{aligned} f_7 &= f_7^* + \frac{1}{12}\rho u + \frac{1}{4}\rho v + \frac{1}{4}\rho w \\ &- \frac{1}{4}(f_3 - f_4) - \frac{1}{4}(f_5 - f_6) + \frac{1}{12}(f_2 - f_1^*) \\ &+ \frac{7}{12}(f_8 - f_7^*) + \frac{1}{12}(f_{10} - f_9^*) \\ &+ \frac{1}{12}(f_{12} - f_{11}^*) - \frac{5}{12}(f_{14} - f_{13}^*) \end{aligned} \tag{30}$$

$$\begin{aligned} f_9 &= f_9^* + \frac{1}{12}\rho u + \frac{1}{4}\rho v - \frac{1}{4}\rho w \\ &- \frac{1}{4}(f_3 - f_4) + \frac{1}{4}(f_5 - f_6) + \frac{1}{12}(f_2 - f_1^*) \\ &+ \frac{1}{12}(f_8 - f_7^*) + \frac{7}{12}(f_{10} - f_9^*) \\ &- \frac{5}{12}(f_{12} - f_{11}^*) + \frac{1}{12}(f_{14} - f_{13}^*) \end{aligned} \tag{31}$$

$$\begin{aligned} f_{11} &= f_{11}^* + \frac{1}{12}\rho u - \frac{1}{4}\rho v + \frac{1}{4}\rho w \\ &+ \frac{1}{4}(f_3 - f_4) - \frac{1}{4}(f_5 - f_6) + \frac{1}{12}(f_2 - f_1^*) \\ &+ \frac{1}{12}(f_8 - f_7^*) - \frac{5}{12}(f_{10} - f_9^*) \\ &+ \frac{7}{12}(f_{12} - f_{11}^*) + \frac{1}{12}(f_{14} - f_{13}^*) \end{aligned} \tag{32}$$

$$\begin{aligned} f_{13} &= f_{13}^* + \frac{1}{12}\rho u - \frac{1}{4}\rho v - \frac{1}{4}\rho w \\ &+ \frac{1}{4}(f_3 - f_4) + \frac{1}{4}(f_5 - f_6) + \frac{1}{12}(f_2 - f_1^*) \\ &- \frac{5}{12}(f_8 - f_7^*) + \frac{1}{12}(f_{10} - f_9^*) \\ &+ \frac{1}{12}(f_{12} - f_{11}^*) + \frac{7}{12}(f_{14} - f_{13}^*) \end{aligned} \tag{33}$$

For D3Q19 model,

$$\begin{aligned} u &= 1 - \frac{f_0 + f_3 + f_4 + f_5 + f_6 + f_{11} + f_{12} + f_{13} + f_{14}}{\rho} \\ &\quad + 2\frac{f_2 + f_8 + f_{10} + f_{16} + f_{18}}{\rho} \end{aligned} \tag{34}$$

$$\begin{aligned} f_1 &= f_1^* + \frac{1}{3}\rho u \\ &+ \frac{1}{3}(f_2 - f_1^* + f_8 - f_7^* + f_{10} - f_9^* \\ &\quad + f_{16} - f_{15}^* + f_{18} - f_{17}^*) \end{aligned} \tag{35}$$

$$\begin{aligned} f_7 &= f_7^* + \frac{1}{6}\rho u + \frac{1}{2}\rho v \\ &- \frac{1}{2}(f_3 - f_4) - \frac{1}{2}(f_{11} - f_{12}) - \frac{1}{2}(f_{13} - f_{14}) \\ &+ \frac{1}{6}(f_2 - f_1^*) + \frac{2}{3}(f_8 - f_7^*) - \frac{1}{3}(f_{10} - f_9^*) \\ &+ \frac{1}{6}(f_{16} - f_{15}^*) + \frac{1}{6}(f_{18} - f_{17}^*) \end{aligned} \tag{36}$$

$$\begin{aligned} f_9 &= f_9^* + \frac{1}{6}\rho u - \frac{1}{2}\rho v \\ &+ \frac{1}{2}(f_3 - f_4) + \frac{1}{2}(f_{11} - f_{12}) + \frac{1}{2}(f_{13} - f_{14}) \\ &+ \frac{1}{6}(f_2 - f_1^*) - \frac{1}{3}(f_8 - f_7^*) + \frac{2}{3}(f_{10} - f_9^*) \\ &+ \frac{1}{6}(f_{16} - f_{15}^*) + \frac{1}{6}(f_{18} - f_{17}^*) \end{aligned} \tag{37}$$

$$\begin{aligned} f_{15} &= f_{15}^* + \frac{1}{6}\rho u + \frac{1}{2}\rho w \\ &- \frac{1}{2}(f_5 - f_6) - \frac{1}{2}(f_{11} - f_{12}) + \frac{1}{2}(f_{13} - f_{14}) \\ &+ \frac{1}{6}(f_2 - f_1^*) + \frac{1}{6}(f_8 - f_7^*) + \frac{1}{6}(f_{10} - f_9^*) \\ &+ \frac{2}{3}(f_{16} - f_{15}^*) - \frac{1}{3}(f_{18} - f_{17}^*) \end{aligned} \tag{38}$$

$$\begin{aligned} f_{17} &= f_{17}^* + \frac{1}{6}\rho u - \frac{1}{2}\rho w \\ &+ \frac{1}{2}(f_5 - f_6) + \frac{1}{2}(f_{11} - f_{12}) - \frac{1}{2}(f_{13} - f_{14}) \\ &+ \frac{1}{6}(f_2 - f_1^*) + \frac{1}{6}(f_8 - f_7^*) + \frac{1}{6}(f_{10} - f_9^*) \\ &- \frac{1}{3}(f_{16} - f_{15}^*) + \frac{2}{3}(f_{18} - f_{17}^*) \end{aligned} \tag{39}$$

The present boundary condition can also be applied to the corner nodes. Consider the top left corner node (Figure 1) of a two dimensional domain, where the unknown distribution functions are f_1, f_4, f_5, f_7 and f_8. It is clear that the distribution functions f_5 and f_7 do not stream from and into the flow domain, but it contributes to the level of the density. Therefore, the density at this location must be specified. Here for simplicity, $f_i^*(\vec{x},\vec{e}_i,t) = f_i(\vec{x},-\vec{e}_i,t)$ is adopted and similar procedure can be applied to other schemes. Thus, the unknown distribution functions adopting Eq. 11 are expressed as $f_1 = f_3 + \omega_1 Q_x$, $f_4 = f_2 - \omega_4 Q_y$, $f_5 = f_7 + \omega_5(Q_x + Q_y)$ and $f_8 = f_6 + \omega_8(Q_x - Q_y)$. f_7 is solved as part of the solution to avoid recursive computation, but $f_7 = f_5 - \omega_7(Q_x + Q_y)$ is still valid. Now, for known ρ, u and v, then

$$\begin{aligned} f_7 &= \frac{\rho - \rho u + \frac{2}{3}\rho v - f_0 - 2(f_2 + f_3 + f_6)}{2} \\ f_1 &= f_3 + \frac{2}{3}\rho u, \qquad f_4 = f_2 - \frac{2}{3}\rho v \\ f_5 &= f_7 + \frac{1}{6}\rho u + \frac{1}{6}\rho v, \qquad f_8 = f_6 + \frac{1}{6}\rho u + \frac{1}{6}\rho v \end{aligned} \tag{40}$$

As expected, for a stationary wall, i.e. $u = v = 0$, this result is the same at that proposed by Zou and He [Zou and He (1997)]. However, the present method can be applied to non-stationary corners. Similar treatments can be applied to other corners for two and three-dimensional flows.

5 Numerical Results

5.1 2-D Poiseuille and Couette-Poisueille flows

Fully developed flow in a channel is a typical case to examine the accuracy of boundary conditions. The Reynolds number is defined as $Re = U_0(2L)/\nu$ in a channel of height $2L$, and U_0 is the maximum velocity. The analytical solution of Poiseuille flow and the maximum relative error are defined as

$$U_{exact} = U_0(1 - \frac{y^2}{L^2}) \tag{41}$$

$$Err_{max} = max(\frac{\sqrt{(u - U_{exact})^2}}{U_0}) \tag{42}$$

Here, the flow driven by a force with periodic boundary condition is examined first, where the proposed velocity boundary conditions are applied on the upper and lower plates of the channel. For this arrangement, the predicted velocity should equal to the exact velocity and the maximum relative error is 6.06448×10^{-11} at

most for the lattice sizes $(8\times4, 16\times8, 32\times16, 64\times32, 128\times64)$. The response of the present boundary condition to the variation of relaxation time τ is also examined using lattice density 4×8. Figure 2 shows the predicted results in comparison with the analytic solution. No slip boundary condition is clearly satisfied and no observable difference among schemes A, B and C exists, which is consistent with the results from Eq. 9.

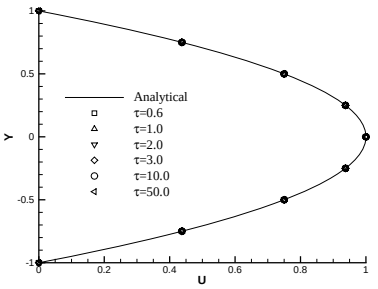

Figure 2: The predicted velocity profiles of Poiseuille flow with different relaxation times.

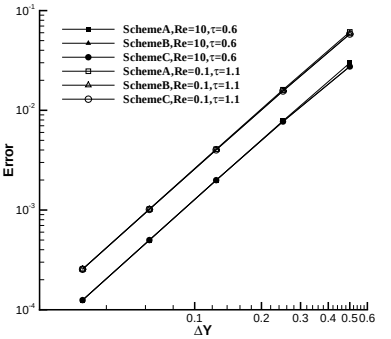

Figure 3: Maximum predicted velocity relative error of Poiseuille flow by D2Q9 model.

Further, pressure driven Poiseuille channel flow is also computed, where mixed pressure velocity boundary conditions are used at the channel inlet and outlet and no slip boundary conditions are applied along the channel walls. The pressure gradient is set as $G = 2\rho\nu U_0/L^2$. Five uniform lattices are used, i.e. $(8\times4, 16\times8, 32\times16, 64\times32, 128\times64)$. Figure 3 shows the predicted results and the second-order accuracy is achieved. It is also interesting to note that the differences among the three schemes A, B and C are negligible.

Then, to highlight capability of the present boundary condition with non-stationary corner, a Couette-Poiseuille flow is simulated. The Reynolds number is defined as $Re = U_0(2L)/\nu$ in a channel of height $2L$, and U_0 is the velocity defined based on the imposed pressure gradient, i.e. $G = 2\rho\nu U_0/L^2$. Besides, the top wall of the channel is moving at a constant velocity $U_{top} = 0.8U_0$ and the bottom wall is stationary. Therefore, the top left and the top right corners both have a velocity of U_{top}. The analytical solution of this Couette-Poiseuille flow and the maximum

relative error are defined as

$$U_{exact} = \frac{1}{2}U_{top}(1+\frac{y}{L}) + U_0(1-\frac{y^2}{L^2}) \tag{43}$$

$$Err_{max} = max(\frac{\sqrt{(u-U_{exact})^2}}{U_{top}}) \tag{44}$$

Four uniform lattices are used, i.e. $(16\times 8, 32\times 16, 64\times 32, 128\times 64)$. Here, Scheme A is applied along wall and corner boundaries. Figure 4 shows the predicted streamwise velocity at the channel inlet and outlet with two Reynolds numbers. As expected, the predicted results agree quite well with the analytic solutions. Also, the maximum relative errors, as shown in Figure 5, indicate that the present non-stationary corner treatment is second order accurate.

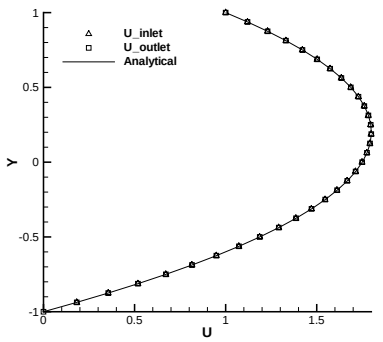

Figure 4: Predicted velocity profiles of Couette-Poiseuille flow.

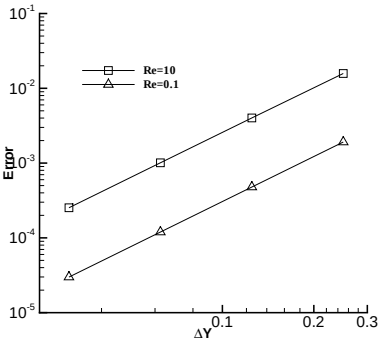

Figure 5: Maximum predicted velocity relative error of Couette-Poiseuille flow.

5.2 Couette flow with wall injection

Next, attention is directed to the Couette flow with wall injection. Here, the channel top wall is moving at a constant velocity U and bottom wall is stationary. Fluid is injected from the bottom wall into the channel and extracted from the top moving wall with a vertical component V_0. No slip boundary conditions (scheme B) are applied along the channel walls and periodic boundary condition is applied at the inlet and outlet.

The Reynolds number is defined based on the injection velocity V_0 and channel height L, i.e. $Re = V_0 L/\nu$. Five different lattice densities in the y direction are

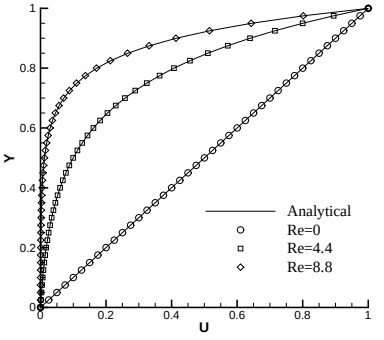

Figure 6: Predicted velocity profiles of Couette flow with wall injection and suction.

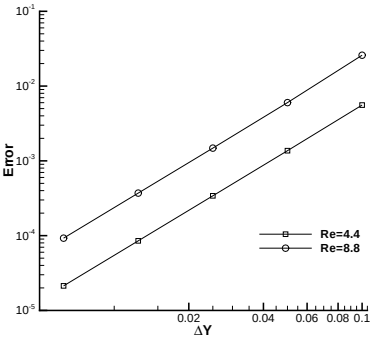

Figure 7: Maximum predicted velocity relative error of Couette flow with wall injection and suction.

adopted, (10, 20, 40, 80, and 160), to determine the convergence rate in space. Figure 6 presents the results compared with the available analytical solution,

$$U_{exact} = U(\frac{e^{(Re\ y/L)} - 1}{e^{Re} - 1}) \tag{45}$$

The influence of the injection velocity can be observed at high Reynolds number case, where at the bottom wall the flow is obstructed by the inward jet. To examine the convergence, equation (42) is used to determine the maximum relative error using different lattices. Figure 7 shows the predicted results are second order accurate for the Reynolds numbers investigated, which is consistent with the results from Eq. 9.

5.3 Lid-driven square cavity flow

2-D lid driven cavity flow is also widely adopted to examine the accuracy of the numerical schemes, where the flow is bounded by a square enclosure and driven by the uniform velocity of the lid. The Reynolds number is defined as $Re = U_0 L/\nu$, where U_0 is the lid velocity and L is the cavity height. The proposed boundary condition (scheme B) is applied to all boundaries to model the flow, where the domain is covered by a lattice size of 256×256. Simulations are conducted at $Re = 100, 400$ and 1000. Predicted horizontal and vertical velocities along the horizontal and vertical wall bisectors are shown in Figures 8 and 9. The simulated results are contrasted with the benchmark solutions of Ghia et al.[Ghia, Ghia, and Shin (1982)] and the agreements are satisfactory.

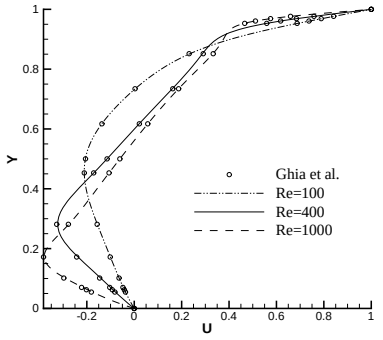

Figure 8: Predicted horizontal velocities of lid-driven cavity flows

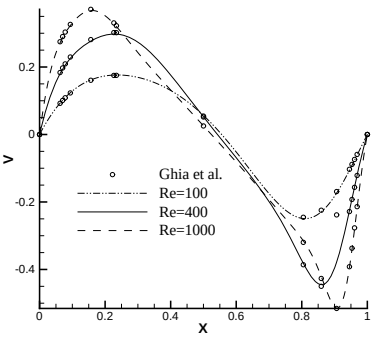

Figure 9: Predicted vertical velocities of lid-driven cavity flows

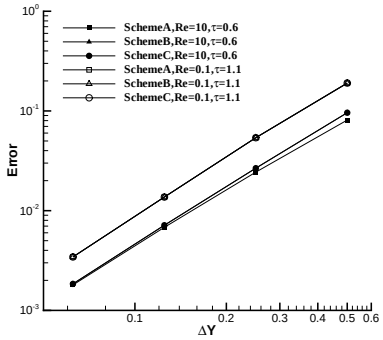

Figure 10: Maximum predicted velocity relative error of 3D Poiseuille flow by D3Q15 model.

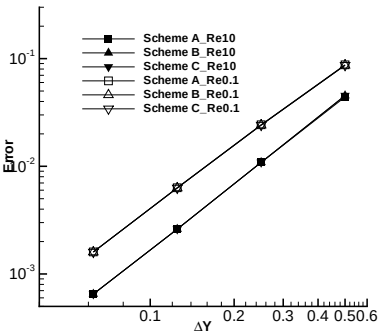

Figure 11: Maximum predicted velocity relative error of 3D Poiseuille flow by D3Q19 model.

5.4 3-D Poiseuille flow in a square duct

The capability of the proposed boundary condition to model three-dimension problem is examined. Here, a pressure driven 3-D square duct flow is simulated by D3Q15 and D3Q19 model. Mixed pressure velocity boundary conditions are applied at the duct inlet and outlet boundary, and no-slip condition is imposed along the bounding walls. The corner treatment is similar to its 2D flow counterpart and is not repeated here. The size of the square duct is $0 \leq x \leq 4L, -L \leq y \leq L$ and $-L \leq z \leq L$, where L is half of the duct height, with x being the flow direction. The

lattice sizes are $N_x \times N_y \times N_z$: $8\times4\times4, 16\times8\times8, 32\times16\times16, 64\times32\times32$. The analytic velocity profile is available for comparison as [White (1991)],

$$u_x(y,z) = \frac{16a^2}{\mu\pi^3}(-\frac{dp}{dx})$$
$$\sum_{i=1,3,5,\ldots}^{\infty}(-1)^{(i-1)/2}[1-\frac{\cosh(i\pi z/2L)}{\cosh(i\pi L/2L)}]\frac{\cos(i\pi y/2L)}{i^3} \tag{46}$$

Two Reynolds numbers are simulated, i.e $Re = 10$ and $Re = 0.1$. The predicted maximum relative errors are shown in Figures 10 and 11. Again, the differences of the adopted schemes are marginal and the results also show second order accuracy. It should be noted, however, that the maximum relative error of D3Q19 is lower than that obtained by D3Q15 model.

6 Conclusion

In this paper, consistent formulations of 2D and 3D pressure and velocity boundary conditions along both the stationary and non-stationary plane walls and corners for lattice Boltzmann simulations are proposed. The unknown distribution functions along the boundary are made function of local known distribution functions and correctors, where the correctors at the boundary nodes are obtained directly from the definitions of density and momentum. In addition, the proposed boundary conditions can be implemented easily for wall and corner boundary using the same formulation. Discrete macroscopic equation is derived for steady fully developed channel flow, and the resulting equation is second order accurate central difference equation, which also implies that the equation produces continuous distribution across the boundary provided the boundary unknown distribution functions satisfy the macroscopic boundary level. Three different boundary condition variants are experimented to assess this assertion and the applicability of the present formulation, and are examined by computing two-dimensional Poiseuille and Couette-Poiseuille flows, Couette flow with wall injection and suction and lid-driven cavity flow and three-dimensional Poiseuille flow within square duct. For the cases investigated, second order accurate solutions are obtained, and the differences of the three boundary formulations are as expected negligible, which is consistent with the discrete macroscopic equation. Thus, the choice of the local known function can be arbitrary, as long as the macroscopic quantity is satisfied.

Acknowledgement: The authors gratefully acknowledge the support by the Taiwan National Science Council (grant 94-2212-E-007-059) and the computational facilities provided by the Taiwan National Center for High-Performance Computing.

References

Chang, C.; Liu, C. H.; Lin, C. A. (2009): Boundary conditions for lattice Boltzmann simulations with complex geometry flows. *International Journal Computers & Mathematics with Applications; doi:10.1016/j.camwa.2009.02.016*.

Chen, C. K.; Chang, S. C.; Sun, S. Y. (2007): Lattice Boltzmann method simulation of channel flow with square pillars inside by the field synergy principle. *CMES: Computer Modeling in Engineering & Sciences*, vol. 22, pp. 203.

Chen, D. J.; Lin, K. H.; Lin, C. A. (2007): Immersed boundary method based lattice Boltzmann method to simulate 2D and 3D complex geometry flows. *International Journal of Modern Physics C*, vol. 18, no. 4, pp. 585.

Chen, S.; Chen, H.; Martinez, D. O.; Matthaeus, W. H. (1991): Lattice Boltzmann model for simulation of magnetohydrodynamics. *Phys. Rev. Lett.*, vol. 67, pp. 3776.

Chen, S.; Doolen, G. D. (1998): Lattice Boltzmann method for fluid flow. *Annular review of fluid mechanics*, vol. 30, pp. 329.

Chen, S.; Martinez, D. O.; Mei, R. (1996): On boundary conditions in lattice Boltzmann methods. *Phys. Fluids*, vol. 8, pp. 2527.

Ghia, U.; Ghia, K. N.; Shin, C. T. (1982): High-Re solutions for incompressible flow using the Navier-Stokes equations and a multigrid method. *Physical Review E*, vol. 48, pp. 387.

Han, K.; Feng, Y. T.; Owen, D. R. J. (2007): Numerical simulations of irregular particle transport in turbulent flows using coupled LBM-DEM. *CMES: Computer Modeling in Engineering & Sciences*, vol. 18, pp. 87.

He, X.; Zou, Q.; Luo, L. S.; Dembo, M. (1997): Analytic solution of simple flows and analysis of nonslip boundary conditions for the lattice Boltzmann BGK model. *J. Stat. Phys.*, vol. 87, pp. 115.

Inamuro, T.; Yoshino, M.; Ogino, F. (1995): A non-slip boundary condition for lattice Boltzmann simulation. *Phys. Fluids*, vol. 7, pp. 2928.

Junk, M.; Yang, Z. X. (2005): One point boundary condition for the lattice Boltzmann method. *Physical Review E*, , no. 066701.

Maier, R. S.; Bernard, R. S.; Grunau, D. W. (1996): Boundary conditions for the lattice Boltzmann method. *Phys. Fluids*, vol. 8, pp. 1788.

Noble, D. R.; Chen, S.; Georgiadis, J. G.; Buckius, R. O. (1995): A consistent hydrodynamic boundary condition for the lattice Boltzmann method. *Phys. Fluids*, vol. 7, pp. 203.

Qian, Y. H.; d'Humieres, D.; Lallemand, P. (1992): Lattice BGK model for Navier-Stokes equation. *Europhysics Letters*, vol. 17, pp. 479.

Skordos, P. A. (1993): Initial and boundary conditions for the lattice Boltzmann method. *Phys. Rev. E*, vol. 48, pp. 4823.

White, F. M. (1991): *Viscous Fluid Flow - 2nd ed.* McGraw-Hill, New York.

Zou, Q.; He, X. (1997): On pressure and velocity boundary conditions for the lattice Boltzmann BGK model. *Phys. Fluids*, vol. 9, pp. 1591.